

# An Improved 360 Degree and Order Model of Venus Topography

NICOLE J. RAPPAPORT, ALEX S. KONOPLIV, AND ALGIS B. KUCINSKAS

*Jet Propulsion Laboratory, California Institute of Technology,  
4800 Oak Grove Drive, Pasadena, California 91109*

AND

PETER G. FORD

*Center for Space Research, Massachusetts Institute of Technology,  
Cambridge, Massachusetts 02139*

*Nicole Rappaport: Tel: (818) 354-8211. Fax: (818) 354-9068.*

*E-mail: Nicole.J.Rappaport@jpl.nasa.gov*

*Alex Konopliv: Tel: (818) 354-6105. Fax: (818) 393-6388.*

*E-mail: ask@krait.jpl.nasa.gov*

*Algis Kucinskis: Tel: (818) 354-4340. Fax: (818) 393-6388.*

*E-mail: algis@chronos.jpl.nasa.gov*

*Peter Ford: Tel: (617) 253-6485. Fax: (617) 253-0861.*

*E-mail: pgf@space.mit.edu*

16 September 1998 — Revised: 29 December 1998

Submitted to *Icarus*, Geodynamics of Venus Special Issue — 18 pages, 10 figures, 3 tables

Key words: topography, spherical harmonics.

Running Title: An Improved 360 Degree and Order Model of Venus Topography

Corresponding Author:

Nicole J. Rappaport  
JPL/Cal Tech  
Mail Stop 301-280  
4800, Oak Grove Drive  
Pasadena, CA 91109

## ABSTRACT

We present an improved 360 degree and order spherical harmonic solution for Venus' topography. The new model uses the most recent set of Venus altimetry data with spacecraft positions derived from a recent high resolution gravity model. Geometric analysis indicates that the offset between the center of mass and center of figure of Venus is about ten times smaller than for the Earth, the Moon, or Mars. Statistical analyses confirm that the rms topography follows a power law over the central part of the spectrum. Compared to the previous topography model, the new model is more highly correlated with Venus' harmonic gravity field.

## I. INTRODUCTION

Together with the gravity field, knowledge of the topography of a planetary body allows researchers to probe its interior density structure (although in a non-unique way). When combined with additional constraints such as surface geology, measurements of topography and gravity can lead to an improved understanding of the planet's thermal evolution. We present a model of Venus topography expanded in spherical harmonic coefficients to degree and order 360. This improves on the previous model of Rappaport and Plaut (1994) by using a Magellan altimetry data set which incorporates updated Magellan spacecraft ephemerides derived from a recent high resolution spherical harmonic model of the Venus gravity field (Konopliv *et al* 1996). The scientific investigations which will benefit from the improved topography model include long-wavelength compensation studies and short-wavelength studies of lithospheric support.

Section II presents the new Venus topography data set. Section III describes the spherical harmonic analysis. In sections IV and V we discuss some geometrical and statistical implications of harmonic modeling. Section VI summarizes our results.

## II. VENUS DATA

### II.1. Improved Spacecraft Ephemeris

When the Magellan spacecraft began mapping in September of 1990, the gravity field of Venus was poorly known, the only information coming from the highly eccentric orbit of the Pioneer Venus Orbiter spacecraft. This resulted in large uncertainties in the determination of Magellan's orbit. As time went on, the JPL navigation team improved its knowledge of the Venus gravity field (McNamee 1992) and the orbital errors were reduced. But by that time, the Magellan ephemeris had been delivered to the science community for use during the first Venus mapping cycle<sup>1</sup>. The radial orbit error<sup>2</sup> for cycle 1 reached several kilometers, mostly during superior conjunction near the end of October 1990. Large radial orbit errors also occurred when the spacecraft's orbital plane

---

<sup>1</sup> One cycle corresponds to moving the spacecraft's periapsis  $360^\circ$  in longitude over the surface of Venus, and lasts approximately 243 days.

<sup>2</sup> The radial direction is that from the center of mass of Venus to the spacecraft.

was face-on as viewed from the Earth since this geometry limited the accuracy of the Doppler tracking technique used to measure line-of-sight velocities.

Figure 1 (a,b,c) shows the original radial position error for each mapping cycle and the improved error using a more recent high resolution gravity model for Venus (model MGNP120PSAAP, Konopliv *et al.* 1996). This model was truncated to degree 90 because the average spacecraft altitude was higher during the first three Magellan mapping cycles where the orbit was not as sensitive to higher degree gravity terms.

The new orbits are computed with 72-hour data arcs, each arc overlapping its neighbors by one orbit (ca. 3.25 hours). The new orbit error displayed in Figure 1 represents the rms differences in the radial spacecraft position in the overlap region between each pair of arcs. The previous orbit solutions had been determined with shorter arc lengths of one day each. In Figure 1, the “old orbit” error is the rms difference between the old and new solutions for the same overlap intervals that were used to determine the “new orbit” errors. Strictly speaking, the orbit errors calculated in this way yield only the *relative* error between orbits and represent a *lower* bound on the absolute error. The absolute error might be significantly greater if a mis-modeling (e.g. in gravity or atmospheric drag) were to affect consecutive arcs in the same way. However, since the “old orbit” errors are also comparable in size to rms differences in overlaps between adjacent old orbit solutions (which used different gravity and drag models), we believe that these values shown in Figure 1 are a good indication of the absolute errors.

Using the improved gravity field and increasing the number of orbits in each solution from 8 to 24 (*i.e.*, from one to three days in one data arc), the sensitivity to the “face-on” geometry has been greatly reduced. Previously, the average radial error had been 20 m, but, during cycle 1 superior conjunction (October 1990), the radial error had at times exceeded 4 km. With the improved gravity field, the maximum error has been reduced to 90 m. Similarly, a radial error of 1 km during a second face-on period in March 1991 has been reduced to 1 m, a value which is now typical of the entire data set. The position errors in other directions has also decreased by an order of magnitude: the typical along-track error from 2 km to 200 m and the normal error (perpendicular to the orbit plane) from 500 m to 50 m.

## II.2. Reprocessed Altimetry Data

The altimeter data set, consisting of measurements of the range from the spacecraft to a total of 4,284,578 surface footprints from 3,971 orbits, has been reanalyzed using the corrected Magellan state vectors. Since the footprint size, which varies from  $8 \times 10$  km at periapsis to  $30 \times 19$  km at the north pole, always exceeded the navigation errors, the principal effect of the improved orbital knowledge was in the radial component, and hence in the values of planetary radii. In some locations, changes of several kilometers were seen. However, the change in the resulting global topographic model is less pronounced since the navigation errors were quite apparent when the original altimetry data were processed and steps were taken at that time to correct them, as described in Ford and Pettengill (1992).

Before gridding the new values of planetary radii, they were first resampled into a rectangular array in which the  $x$ -axis represented orbit number and the  $y$ -axis represented surface-fixed footprint latitude. The columns were then sorted by periapsis longitude, bringing together data points taken at multiples of 243 days apart. Since the Magellan altimeter observed almost 3 full cycles, any remaining navigation errors might be expected to show up as a systematic pattern of high and low radius values. Using a spatial filter matched to the characteristics of this pattern, the navigation errors can be isolated and subtracted from the individual footprint radii before gridding.

This technique was highly successful in reducing the effect of navigation errors in the original model, but was found to be unnecessary for the new navigation solutions since the corrections, now very much smaller, were found to be comparable in size to the leakage of genuine high-frequency topography through the matched filter. It was therefore decided *not* to apply the filter to the topography model itself, but to use it instead to estimate an upper bound on remaining systematic errors. Figure 2 shows the rms of these error estimates combined with the statistical errors associated with the detection of the radar echo. The average radius error is 16.1 m, dominated by the high values that cluster around 240E longitude, where the spacecraft orbit was nearly orthogonal to the Earth-Venus vector during the mapping cycle 1. By comparison, the average error from the previous analysis was 39.5 m.

The final stage in building the altimetry data set was to resample the footprint radii into a cartographic array. The pixel size was  $5 \times 5$  km, and each footprint contributed a weight based on (a) its statistical echo-detection error, (b) the “goodness of fit” of the echo to a suite of pre-calculated echo templates, and (c) the footprint size, modeled

as Gaussian functions along and across the sub-radar track. This technique has been used to generate the previous model, but an additional step has been added – if the radar echo is accompanied by a precursor containing more than 20% of the power and arriving more than  $3.3 \mu\text{sec}$  (i.e., 1 km) in advance of the primary component, that footprint is discarded. This procedure is effective at removing noisy measurements in areas of extreme topographic contrast. At long wavelengths, the resulting image differs little from the previous analysis – the mean radius has changed from 6051.84 km to 6051.88 km, and the depths of some of the deeper chasmata<sup>3</sup> have decreased as a direct result of discarding the multi-component echoes. The topographic data set obtained by this procedure is significantly improved with respect to previous versions. A  $5 \times 5$  km gridded image will be submitted to the National Space Sciences Data Center, Greenbelt, MD, as a Global Topographic Data Record (GTDR), product ID GTDR.3;2 (digital) and GTDRP.3;3 (photo).

### II.3. Topography Data

A  $0.25^\circ \times 0.25^\circ$  grid of Venus radii was obtained by projecting and averaging the improved GTDR. This reduces the resolution, especially at low latitudes, so that every sample is based on the average of several Magellan altimetry data points. The results are referenced to the Venus body-fixed reference frame (Davies *et al* 1992).

Figure 3 shows a  $1^\circ \times 1^\circ$  resolution map of the difference of each grid point between the “old” and the “new” Magellan topography data. Radial errors that have been removed in the new data show up as either positive or negative valued streaks. Most noteworthy are two strong south-trending bands, one starting to the East of Maxwell Montes ( $10^\circ\text{E}$ ,  $70^\circ\text{N}$ ), the other starting at about  $120^\circ\text{W}$ ,  $60^\circ\text{N}$ . As expected, radial error streaks are most pronounced during superior conjunction (i.e., when Venus moves behind the Sun and Doppler tracking becomes ineffective) and when the orbit moves into the “plane of the sky” (i.e., presents a face-on orbit geometry). The pattern of predominately yellow dots that follow contours in Figure 3 are the result of small shifts in footprint location due to changes in ephemeris from one navigation solution to the other.

---

<sup>3</sup> Chasmata are broad valleys, troughs, or depressions.

### III. HARMONIC ANALYSIS

In this section we present the approach used to produce the spherical harmonic Venus topography model from gridded Magellan data, as well as the results of this harmonic analysis.

We use the  $0.25^\circ \times 0.25^\circ$  topography array to produce a new spherical harmonic model of topography. This approach is intuitively justified by the behavior of harmonic functions, since each such function has the same number of zeroes on each parallel. Each grid point is therefore weighted by the area of the corresponding cell. The planetary radius at latitude  $\varphi$  and longitude  $\lambda$  with respect to the body-fixed reference frame defined by Venus' rotation axis and prime meridian can be modeled as a double series expansion in spherical harmonic functions written as

$$R(\varphi, \lambda) = R_t \sum_{\ell=0}^{+\infty} \sum_{m=0}^{\ell} P_{\ell m}(\sin \varphi) (C_{\ell m}^t \cos m\lambda + S_{\ell m}^t \sin m\lambda), \quad (1)$$

where  $R_t$  is a reference radius,  $C_{\ell m}^t$  and  $S_{\ell m}^t$  are the corresponding normalized harmonic coefficients of the topography, and  $P_{\ell m}$  are the normalized Legendre functions.

We followed the method of Rappaport and Plaut (1994) and used numerical quadrature to compute the harmonic coefficients of Venus topography to degree and order 360 from the new data grid of Magellan planetary radii. This is more computationally efficient than the method of least squares, especially for large values of  $\ell$ .

The mean radius and spherical harmonic coefficients of equation (1) were computed as individual integrals over the planet's surface to degree and order 360. The harmonic coefficients up to degree 5 are listed in Table I. The complete spherical harmonic model can be obtained from the Planetary Data System (PDS) Geosciences Node archive at Washington University, St. Louis, MO, or by writing directly to the authors of this paper.

The mean Venus' radius (defined so that  $C_{00} = 1$ ) is found to be  $R_t = 6051.881$  km. The previous estimate of Rappaport and Plaut (1994) was  $R_t = 6051.848$  km. The difference between these values is entirely due to the improvement in altimetry data which is, in turn, principally due to the reduction in navigation errors, as explained in section II.



Figure 4 illustrates our new topography model as an image of the variation in topography, relative to  $R_t$ , derived from the spherical harmonics. Figure 5 shows the topography along the equator at a resolution of  $1^\circ$ , both as given by the new gridded topography data (continuous line) and as computed from the new harmonic solution (crosses), indicating a good agreement between the model and the data. Figure 6 contains the difference between the two plots of Figure 5, showing that the errors in the model are dominated by high frequency components.

#### IV. GEOMETRICAL IMPLICATIONS

It has been traditional to define the center of figure in one of two ways: (i) the center of a sphere approximating the shape of the planetary body; (ii) the center of an ellipsoid approximating its shape. For a slowly rotating body like Venus, with a low  $J_2$ , (i) is superior for most geophysical interpretations, but (ii) is often preferred when establishing data bases of planetary parameters (e.g., for use in future planetary missions). We selected approach (ii), recognizing that the center of figure for approach (i) is easily derived from the harmonic coefficients of degree 1.

In this work, we fitted by least squares an offset ellipsoid to a  $1^\circ \times 1^\circ$  grid of Venus' topography that was computed by interpolating the  $0.25^\circ \times 0.25^\circ$  gridded data. The nine parameters that were fitted were (a) the coordinates  $x_f, y_f, z_f$  of the center of figure with respect to the Venus body-fixed reference frame (Davies *et al* 1992), (b) the Euler angles  $\psi, \theta, \varphi$  orienting the principal axes with respect to the reference frame centered at the center of figure and translated from the Venus body-fixed reference frame (Davies *et al* 1992), and (c) the lengths  $A, B$ , and  $C$  of the ellipsoid's semi-axes. The fit minimized the sum of the squares of the residuals  $(X/A)^2 + (Y/B)^2 + (Z/C)^2 - 1$ , where  $X, Y$  and  $Z$  denote the grid point coordinates with respect to the translated and rotated reference frame. The principal difficulty lies in selecting the initial conditions of the least squares fit. Our method to compute the initial conditions involves the following 4 steps:

1. Compute the spherical harmonic coefficients of Venus topography by least squares to degree and order 2.

2. Use the obtained mean radius of Venus and the harmonic coefficients of degree 1 of the topography to compute an approximate location of the center of figure. We obtained:

$$\begin{aligned}
 x_f &= R_t C_{11} = -56.9 \text{ m}, \\
 y_f &= R_t S_{11} = 177.3 \text{ m}, \\
 z_f &= R_t C_{10} = 9.0 \text{ m}.
 \end{aligned}
 \tag{2}$$

3. Use the harmonic coefficients of degree 2 of the topography to compute a matrix formally similar to the inertia tensor computed from the harmonic coefficients of degree 2 of the gravity field. We solved for the rotation that diagonalizes that matrix to compute approximate Euler angles, obtaining:

$$\begin{aligned}
 \psi &= -101.02^\circ, \\
 \theta &= 27.00^\circ, \\
 \varphi &= 102.91^\circ.
 \end{aligned}
 \tag{3}$$

4. Finally, choose arbitrarily initial conditions for  $A$ ,  $B$  and  $C$ :

$$\begin{aligned}
 A &= 6060 \text{ km}, \\
 B &= 6050 \text{ km}, \\
 C &= 6040 \text{ km}.
 \end{aligned}
 \tag{4}$$

Having selected the initial conditions, we performed the least squares fit. It used the full topography data and converged to the following solution:

$$\begin{aligned}
x_f &= -56.9 \text{ m}, \\
y_f &= 177.4 \text{ m}, \\
z_f &= 9.2 \text{ m}, \\
\psi &= -101.01^\circ, \\
\theta &= 27.03^\circ, \\
\varphi &= 102.93^\circ, \\
A &= 6051.9556 \text{ km}, \\
B &= 6052.2968 \text{ km}, \\
C &= 6051.3673 \text{ km}.
\end{aligned} \tag{5}$$

The latitudinal coordinates of the center of figure are:

$$\begin{aligned}
r_f &= 186.5 \text{ m}, \\
\varphi_f &= 2.8^\circ, \\
\lambda_f &= 107.8^\circ,
\end{aligned}$$

which indicates that the center of figure lies close to the Venus equatorial plane under the north-west corner of Thetis Regio in Aphrodite Terra.

The orientation of the axes of figure and of the axes of inertia using the MGNP180U.ODP gravity field model are given in Table II. The two sets of axes do not coincide, which indicates a weak correlation between Venus' shape and its inertia properties. The orientation of the axes of figure is governed by the equatorial and mid-latitude highlands. The largest axis of figure passes through Phoebe Regio and Ovda Regio in western Aphrodite Terra. The second axis of figure passes through Eistla Regio and south west of Atla in eastern Aphrodite Terra.

## V. STATISTICAL IMPLICATIONS

The statistical nature of the topography field is conveniently summarized by the rms degree magnitudes of the normalized spherical harmonic coefficients, defined as

$$\text{rms}(\ell) = \sqrt{\frac{\sum (C_{\ell m}^t)^2 + (S_{\ell m}^t)^2}{2\ell + 1}}, \tag{6}$$

where the sum is from  $m = 0$  to  $\ell$ . Figure 7 shows the rms magnitude spectrum, plotted on a logarithmic scale, for the global topography of Venus (solid line) and Earth (dotted line), with degree from  $\ell = 2$  to  $\ell = 360$ . The Venus spectrum is that of the harmonic model presented in this paper, and the Earth spectrum is from the “equivalent rock topography” model of Rapp and Pavlis (1990).

As noted by Rappaport and Plaut (1994), the slope of the Venus topography spectrum changes as  $\ell > \simeq 100$ , becoming flatter. This may not be a real property of the spectrum but rather an artifact associated with the method used to compute the harmonic coefficients. Indeed, as was mentioned in section III, the errors in the topography model are essentially restricted to the high frequency terms.

Over the  $\ell \simeq 3$  to  $\ell \simeq 100$  degree interval, Venus and Earth topography correspond quite closely to a power-law spectral correlation. However, we note that the Venus spectrum has significantly lower amplitudes and a slightly shallower slope than does the Earth, as noted by other authors (Kaula 1984; Turcotte, 1987; Kucinskas and Turcotte, 1994). Kaula (1984) and Kucinskas and Turcotte (1994) attributed this to a predominance of “rolling plains” topography on Venus, where more than 80% of the planet’s surface lies within 1 km of the mean planetary radius.

Figure 8 compares the rms degree magnitude spectrum of the new Venus topography (circles) with the harmonic rms difference spectrum between the “new” and “old” Venus topography models (stars). The y-axis offset between the two curves provides an upper bound on the errors associated with the topography model. We also compared the variance of the observed topography with the variance of the topography computed from our model. Denoting the topography by  $f$ , the variance was computed using

$$\sigma_f = \frac{1}{S} \int_{-\pi/2}^{\pi/2} \int_0^{2\pi} [f(\varphi, \lambda) - \bar{f}]^2 dS, \quad (7)$$

where  $dS$  represents an element of surface and

$$\bar{f} = \frac{1}{S} \int_{-\pi/2}^{\pi/2} \int_0^{2\pi} f(\varphi, \lambda) dS. \quad (8)$$

With the observed topography, we obtained  $\sqrt{\sigma_f} = 0.966$  while our model gives a value of  $\sqrt{\sigma_f} = 0.958$ . The agreement between these two values is due to the fact that

the variance is essentially due to the low degree terms and it may be that the model overestimates the power of the high degree harmonic coefficients.

The gravitational potential at a point  $P$  outside the planet can be written, in terms of spherical harmonic coefficients, as

$$U(r, \varphi, \lambda) = \frac{GM}{r} \sum_{\ell=2}^{+\infty} \sum_{m=0}^{\ell} \left( \frac{R_g}{r} \right)^{\ell} P_{\ell m}(\sin \varphi) (C_{\ell m}^g \cos m\lambda + S_{\ell m}^g \sin m\lambda), \quad (9)$$

where  $G$  is the gravitational constant,  $M$  is the mass of the planet,  $R_g$  is a reference radius, and the  $C_{\ell m}^g$ ,  $S_{\ell m}^g$  are the harmonic coefficients for degree  $\ell$  and order  $m$ . As a quantitative measure of the correlation between the gravity and topography, one can define the degree functional correlation as

$$\gamma(\ell) = \frac{\sum C_{\ell m}^t C_{\ell m}^g + S_{\ell m}^t S_{\ell m}^g}{\sqrt{\sum (C_{\ell m}^t)^2 + (S_{\ell m}^t)^2} \sqrt{\sum (C_{\ell m}^g)^2 + (S_{\ell m}^g)^2}}, \quad (10)$$

where the sum goes from  $m = 0$  to  $\ell$ . The correlation per degree is shown in Figure 9 for two topography models, the dotted line representing Rappaport and Plaut (1994), and the solid line refers to the model presented in this paper. Both calculations used the most recent 180 degree and order gravity field model MGNP180U.ODP of Konopliv *et al.* (1998). Our new topography model has the higher correlation with the gravity field throughout most of the degree spectrum. Assuming that a higher correlation is a measure of success, our result reflects the improvements over the previous topography harmonic model.

Regional functional correlations were computed in the following way. Denoting the gravity at the surface by  $g$  and using equations (8) and (7) to compute  $\bar{g}$  and  $\sigma_g$ , the regional correlation is given by

$$\gamma = \frac{\frac{1}{S} \int \int (f - \bar{f})(g - \bar{g}) dS}{\sqrt{\sigma_f \sigma_g}}. \quad (11)$$

Regional correlations over seven regions of Venus are listed in Table III for the topography and gravity models used in Rappaport and Plaut (1994) as well as for the topography model presented in this paper, each correlated against the new gravity model MGNP180U.ODP. For the comparison to be meaningful, the new topography and

gravity models were truncated to degree and order 60. No filtering other than removing the coefficients of degree and order higher than 60 was applied. No tapering was applied to the topography because the coefficients, which were computed by quadrature, are independent of each other. Consistently, the same treatment was applied to the gravity. The new models are seen to give improved correlations.

Among the seven regions studied, the highest correlations were found in Beta Regio and Atla Regio (Rappaport and Plaut, 1994). These highlands are also characterized by moderate negative Bouguer anomalies and abundant volcanism, suggesting thermal and/or dynamic support of the topography (e.g., Smrekar and Phillips, 1991; Grimm and Phillips, 1992; Kucinskas and Turcotte, 1994; Simons *et al*, 1994; Moore and Schubert, 1995; Kucinskas, 1996; Simons *et al*, 1997). The lowest correlation was obtained in Ovda Regio, which is characterized by very large negative Bouguer anomalies and complex ridged terrain or tessera, suggesting an essentially passive isostasy associated with crustal thickening (e.g., Smrekar and Phillips, 1991; Kucinskas and Turcotte, 1994; Simons *et al*, 1997).

Using our new topography harmonic solution as well as the new Venus gravity solution of Konopliv *et al.* (1998), we computed degree geoid to topography ratios (GTR). The degree GTR is defined as the ratio of the degree variances of the harmonic spectra of the topography and geoid derived from the gravity model (Kucinskas and Turcotte 1994; Kucinskas 1996). The degree variances of the harmonic spectra were defined as in Turcotte (1987) and Rapp (1989), yielding degree GTR in units of meters per kilometer.

In Figure 10 we use a log-linear scale to plot the degree GTR versus degree  $\ell$  for the new topography and gravity models as well as for the new topography model and a Bouguer gravity model corresponding to the uncompensated topography. To generate the Bouguer gravity we used a rock density  $\rho_c = 2.9\text{gcm}^{-3}$ . It can be seen from the figure that the GTRs for the uncompensated topography are significantly larger for all  $\ell$  than the observed GTR values. This result, combined with the strong correlation observed between gravity and topography for Venus, implies that much of the observed anomaly of Venus geoid can be directly associated with compensated topography. However, because of the non-unique association of gravity with internal mass distribution, this can be interpreted as indicating that either a significant portion of the topography is isostatically supported at depth (e.g., Kucinskas and Turcotte, 1994) or that much of

the topography is maintained dynamically (*e.g.*, Simons *et al.* 1997). For a description of how the effective depth of isostatic compensation required to match the observed GTR varies across the spectrum the reader is referred to Figure 13 of Sjogren *et al* (1997).

## VI. SUMMARY

This paper describes a new spherical harmonic model of Venus topography. The model improves on the prior solution by incorporating corrections introduced by improved Magellan spacecraft positions and refined altimetric data reduction. Geometrical and statistical analyses indicate that:

- (a) The offset between the center of mass and the center of figure is about ten times smaller than that of the Earth, the Moon, or Mars. The center of figure of Venus lies under Aphrodite Terra.
- (b) The orientation of the principal axes of figure is determined by the equatorial and mid-latitude highlands.
- (c) The rms spectrum of the topography follows a power law up to degree  $\ell \sim 100$ . The flattening of the spectrum for  $\ell > 100$  may not be real. The Venus topography spectrum has lower amplitudes and a slightly shallower spectral slope than that of Earth. This may be due to the "rolling plains" topography which dominates on the planet.
- (d) The Venus topography and gravity fields are very strongly, positively, correlated with the exception of degree 2. Regional correlations are higher in Beta and Atla Regiones – thought to be dynamically and/or thermally supported – than in Ovda Regio which may be mainly isostatically supported via crustal thickening (*e.g.*, Smrekar and Phillips, 1991; Grimm and Phillips, 1992; Kucinskas and Turcotte, 1994; Simons *et al*, 1994; Moore and Schubert, 1995; Kucinskas, 1996; Simons *et al*, 1997).
- (e) A degree analysis of the GTR for the new topography and gravity harmonic models, together with the correlation results, show that Venusian topography is substantially compensated.

## ACKNOWLEDGMENTS

Part of this research was performed at the Jet Propulsion Laboratory, California Institute of Technology, under contract to the National Aeronautics and Space Administration. It was also funded by NASA Planetary Geology and Geophysics Grants 344-30-53-02 and NAG5-4047, and by JPL subcontract 960510.



## REFERENCES

- Davies, M.E., V.K. Abalakin, M. Bursa, T. Lederle, J.H. Lieske, R.H. Rapp, P.K. Seidelman, A.T. Sinclair, V.G. Teifel and V.S. Tjuflin 1992. Report of the IAU/IAG/COSPAR working group on cartographic coordinates and rotational elements of the planets and satellites: 1991. *Celes. Mech.* **53**, 377–397.
- Ford, P.G. and G.H. Pettengill 1992. Venus topography and kilometer-scale slopes. *J. Geophys. Res.* **97**, 13,103–13,114.
- Grimm, R.E. and R.J. Phillips 1992. Anatomy of a Venusian hot spot: Geology, gravity, and mantle dynamics of Eistla Regio. *J. Geophys. Res.* **97**, 16,035–16,054.
- Kaula, W.M. 1984. Tectonic contrasts between Venus and the Earth. *Geophys. Res. Lett.* **11**, 35–37.
- Konopliv, A.S., W.L. Sjogren, C.F. Yoder, and E. Carranza 1996. Venus 120th degree and order gravity field. 1996 AGU Fall Meeting, San Francisco, CA.
- Konopliv, A.S., W.B. Banerdt and W.L. Sjogren 1998. Venus gravity: 180th degree and order model. Submitted to *Icarus*.
- Kucinskas, A.B., and D.L. Turcotte 1994. Isostatic compensation of equatorial highlands on Venus. *Icarus* **112**, 104–116.
- Kucinskas, A.B. 1996. Compensation of the Venus highlands: an isostatic approach. Ph.D. dissertation, Cornell University, Ithaca, NY.
- McNamee, J.B., G.R. Kronschnabl, S.K. Wong, and J.E. Ekelund 1992. A gravity field to support Magellan navigation and science at Venus. *J. Astron. Sci.* **40**, 107–134.
- Moore, W.B. and G. Schubert 1995. Lithospheric thickness and mantle /lithosphere density contrast beneath Beta Regio, Venus. *Geophys. Res. Lett.* **22**, 429–432.
- Rapp, R.H. 1989. The decay of the spectrum of the gravitational potential and the topography for the Earth. *Geophys. J. Int.* **99**, 449–455.
- Rapp, R.H., and N.K. Pavlis 1990. The development and analysis of geopotential coefficient models to spherical harmonic degree 360. *J. Geophys. Res.* **95**, 21,885–21,911.

- Rappaport, N.J. and J.J. Plaut 1994. A 360 degree and order model of Venus topography. *Icarus* **112**, 27–33.
- Simons, M., B.H. Hager, and S.C. Solomon 1994. Global variations in geoid topography admittances of Venus. *Science* **256**, 798–803.
- Simons, M., S.C. Solomon, and B. H. Hager 1997. Localization of gravity and topography: constraints on tectonics and mantle dynamics of Venus. *Geophys. J. Int.* **131**, 24–44.
- Sjogren, W.L., W.B. Banerdt, P.W. Chodas, A.S. Konopliv, G. Balmino, J.P. Barriot, J. Arkani-Hamed, T.R. Colvin, and M.E. Davies 1997. In *Venus II* (S.W. Bougher, D.M. Hunten, and R.J. Phillips, Ed.), pp. 1, 125–1, 161, Univ. of Arizona Press, Tucson.
- Smrekar, S.E., and R.J. Phillips 1991. Venusian highlands: Geoid to topography ratios and their implications. *Earth Planet. Sci. Lett.* **107**, 582–597.
- Turcotte, D.L. 1987. A fractal interpretation of topography and geoid spectra on the Earth, Moon, Venus, and Mars. *Proc. Lunar Planet. Sci. Conf. 17th, Part 2. J.Geophys. Res.* **92**, (Suppl.), E597–601.

$\ell$	$m$	$C_{\ell m}$	$S_{\ell m}$
1	0	$(-1.3773) \times 10^{-6}$	
1	1	$(-1.9327) \times 10^{-5}$	$(1.7113) \times 10^{-5}$
2	0	$(-2.6938) \times 10^{-5}$	
2	1	$(1.5447) \times 10^{-5}$	$(-7.9224) \times 10^{-6}$
2	2	$(-2.2297) \times 10^{-5}$	$(3.7788) \times 10^{-7}$
3	0	$(3.0154) \times 10^{-5}$	
3	1	$(4.8880) \times 10^{-5}$	$(-8.0741) \times 10^{-6}$
3	2	$(5.1822) \times 10^{-6}$	$(2.4327) \times 10^{-5}$
3	3	$(-5.3683) \times 10^{-6}$	$(-4.3631) \times 10^{-6}$
4	0	$(2.7921) \times 10^{-5}$	
4	1	$(6.6142) \times 10^{-6}$	$(1.4978) \times 10^{-5}$
4	2	$(1.6065) \times 10^{-5}$	$(9.2011) \times 10^{-6}$
4	3	$(-4.5104) \times 10^{-6}$	$(-3.5665) \times 10^{-6}$
4	4	$(8.4460) \times 10^{-6}$	$(2.9252) \times 10^{-5}$
5	0	$(-9.5343) \times 10^{-6}$	
5	1	$(2.0833) \times 10^{-5}$	$(2.3408) \times 10^{-5}$
5	2	$(4.7354) \times 10^{-6}$	$(-1.4049) \times 10^{-5}$
5	3	$(8.6703) \times 10^{-6}$	$(1.9919) \times 10^{-5}$
5	4	$(9.4196) \times 10^{-6}$	$(1.7517) \times 10^{-6}$
5	5	$(8.2753) \times 10^{-6}$	$(-6.4849) \times 10^{-6}$

**Table I:** Normalized harmonic coefficients of the topography to degree and order 5.

	Axes of Figure	Axes of Inertia
Latitude Longitude Length	$-5.8^\circ$ $90.5^\circ$ 6052.3 km	$0.3^\circ$ $-3.2^\circ$
Latitude Longitude Length	$26.3^\circ$ $3.4^\circ$ 6052.0 km	$0.3^\circ$ $86.8^\circ$
Latitude Longitude Length	$63.0^\circ$ $169.0^\circ$ 6051.4 km	$89.5^\circ$ $220.3^\circ$

**Table II:** Orientation of the principal axes of figures and of the principal axes of inertia of Venus.

Regio	$\varphi_{min}$	$\varphi_{max}$	$\lambda_{min}$	$\lambda_{max}$	$\gamma_{old}$	$\gamma_{new}$
BETA	10°	40°	-105°	-55°	0.934	0.935
PHOEBE	-25°	10°	-90°	-50°	0.845	0.857
MAXWELL	45°	80°	-60°	30°	0.864	0.881
GULA	0°	30°	-15°	30°	0.918	0.955
BELL	0°	40°	30°	60°	0.812	0.855
OVDA	-15°	10°	75°	110°	0.805	0.811
ATLA	-10°	30°	180°	210°	0.968	0.973
PLANET	-90°	90°	-120°	240°	0.772	0.801

**Table III:** Correlations between Venus' topography and its gravity field over seven regions and over the entire planet;  $\gamma_{old}$  is derived from for the previous topography and gravity models used in Rappaport and Plaut (1994);  $\gamma_{new}$  is based on this paper's topography and gravity models; for comparison, all models were truncated at degree and order 60.

## FIGURE CAPTIONS

FIGURE 1: Navigation radial position rms errors, old and new, for Magellan Cycle 1 (a), cycle 2 (b), and cycle 3 (c).

FIGURE 2: Image of the residual errors (rms estimated errors) in the new Magellan topography.

FIGURE 3: Map of the difference between the old and new gridded Magellan topography.

FIGURE 4: Topography map produced from this paper's  $360 \times 360$  topography model. The zero level correspond to the Venus mean radius  $R_t = 6051.881$  km. The topography contours are at 1 km intervals.

FIGURE 5: Topography along the equator from the new data (continuous line) and as computed from our new model (crosses), with respect to the reference radius. The vertical scale is in kilometers.

FIGURE 6: Difference between the topography along the equator computed from the model and the observed topography. The vertical scale is in kilometers.

FIGURE 7: Rms magnitude of the normalized coefficients of the topography of Venus (solid line) and Earth (dotted line) on a logarithmic scale.

FIGURE 8: Rms magnitude spectrum of the new Venus topography (circles) and the difference between the new and old Venus topography (stars).

FIGURE 9: Correlation per degree between Venus' topography and its gravity field, comparing the topography model of Rappaport and Plaut (1994) (dotted correlation line), and this paper's topography model (solid correlation line); all calculations use the most recent gravity field model of Konopliv *et al.* (1998).

FIGURE 10: Degree geoid to topography ratios (GTRs) for Venus data plotted versus degree  $\ell$ . The open circles are for observed data and the solid curve is for an uncompensated topography model (see text).

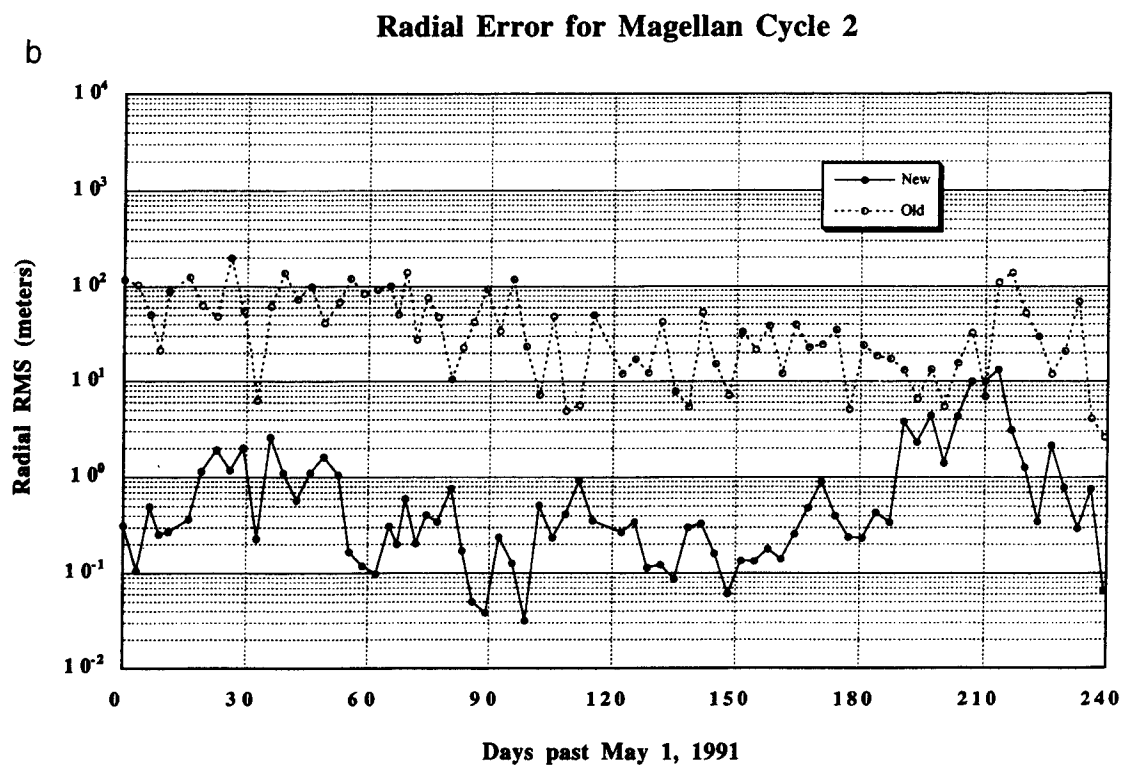
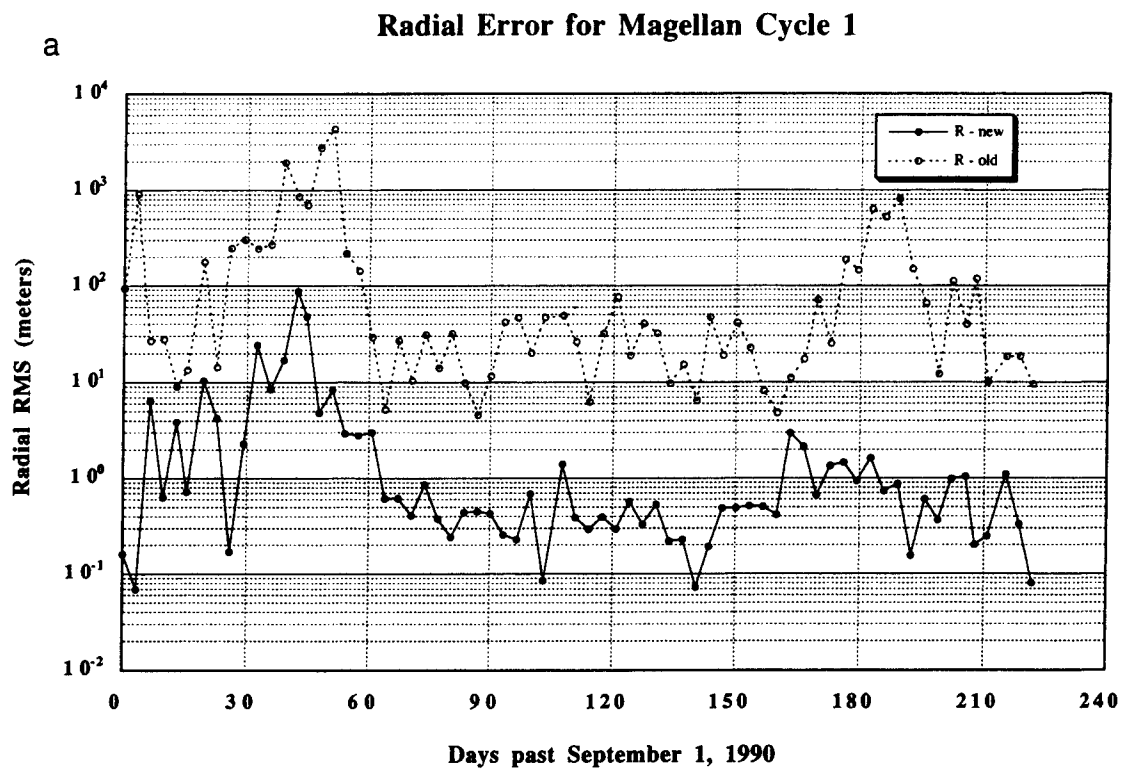
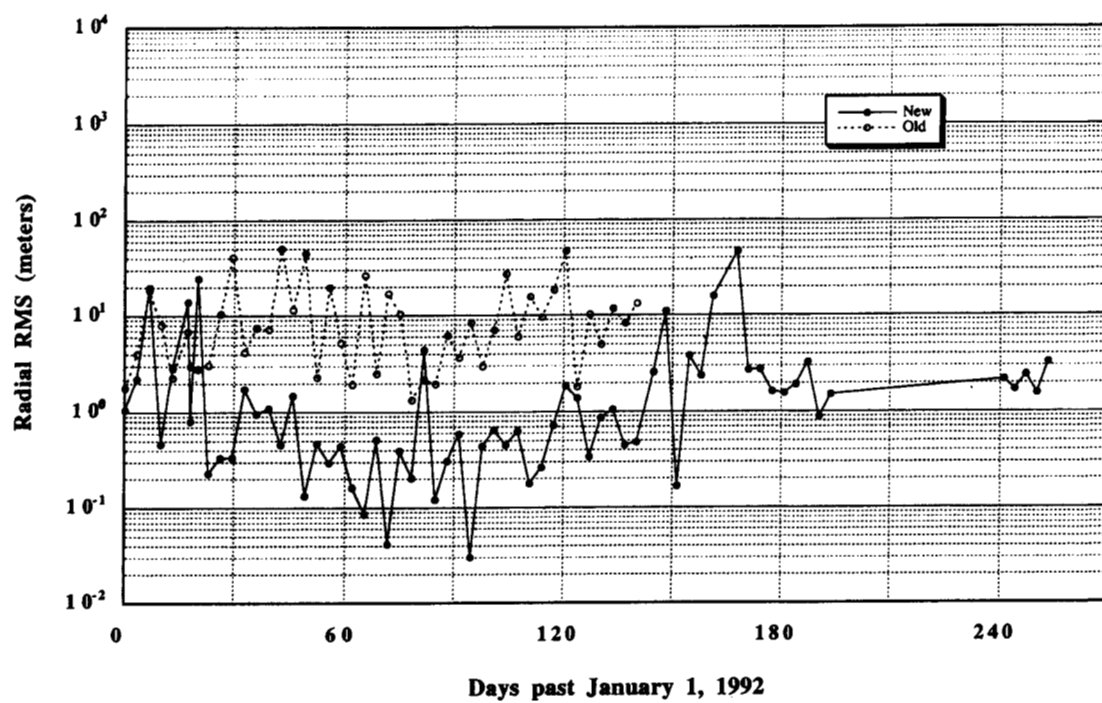


FIG. 1. Navigation radial position RMS errors, old and new, for Magellan cycle 1 (a), cycle 2 (b), and cycle 3 (c).

C

### Radial Error for Magellan Cycle 3

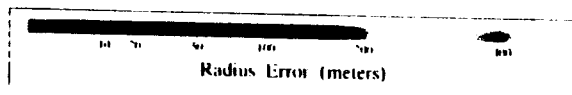
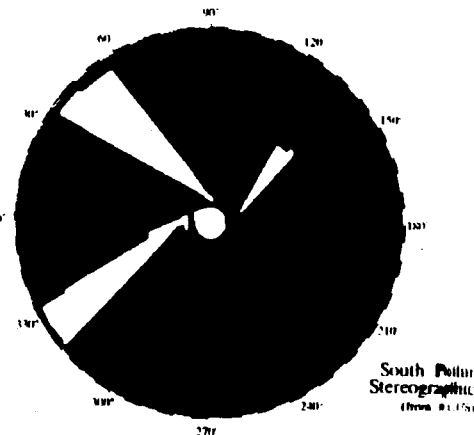
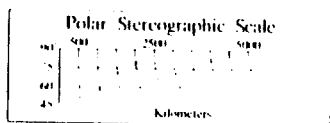
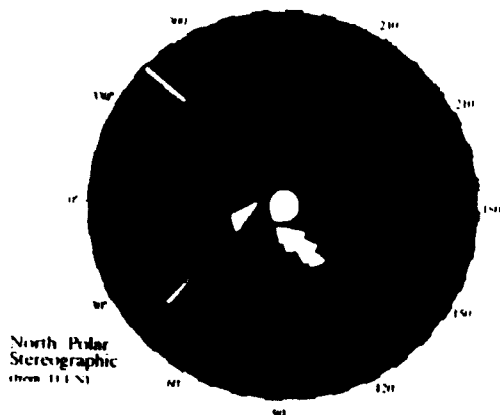




MAGELLAN

VENUS TOPOGRAPHY ERROR

GTEDRP.3.2



PRODUCT ID: GTEDRP.3.2  
STARTING ORBIT: 376  
ENDING ORBIT: 5747  
PREFI SIZE: 5x5 km

PRODUCTION DATE: 02/10/98  
PRODUCTION TIME: 09:48:27  
HARDWARE VERSION: 01  
SOFTWARE VERSION: 02

FIGURE 2

# Venus Topography: new data - old data

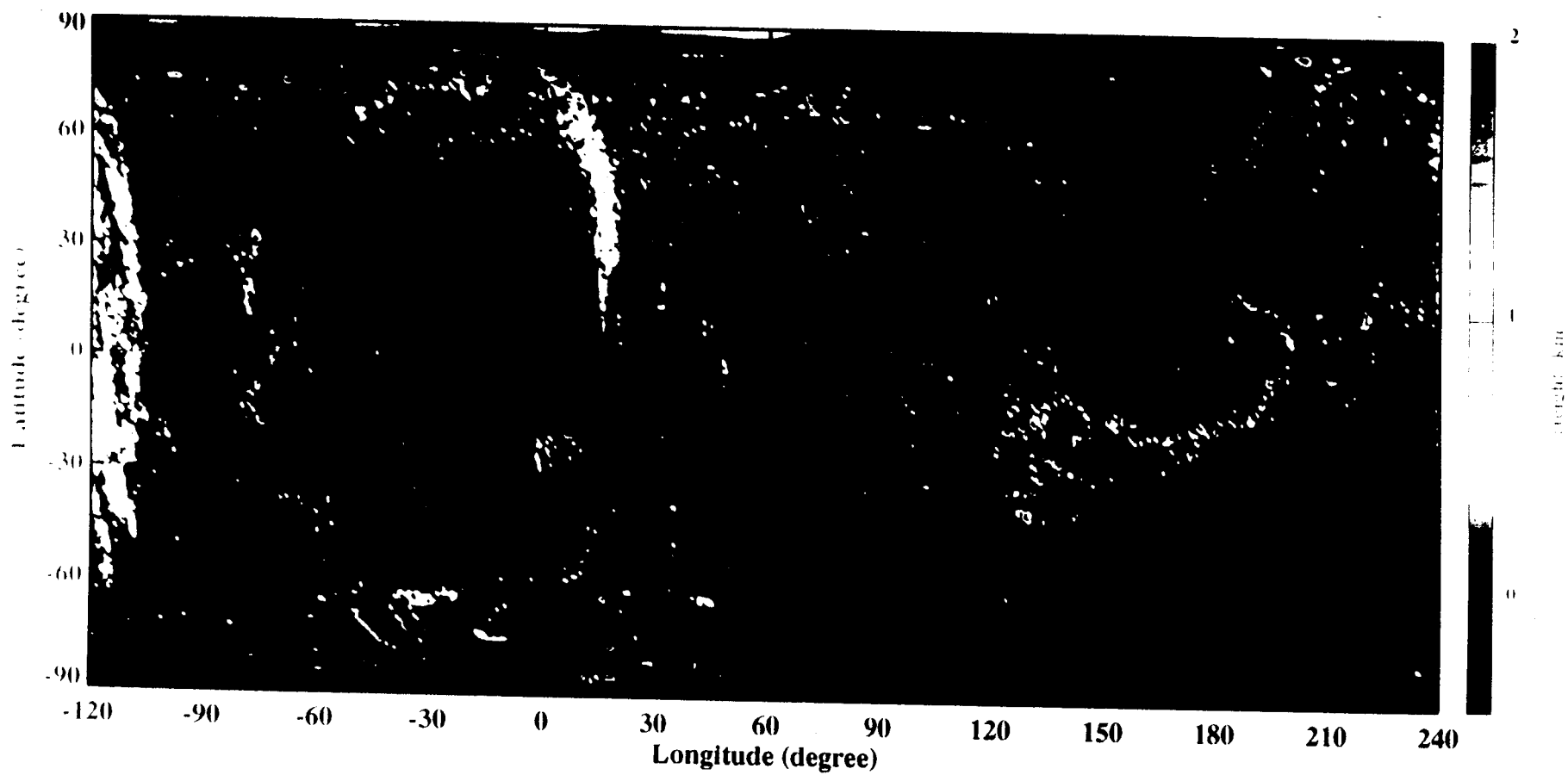


FIGURE 3

**Venus Topography: 360 degree and order model  
(from gtdr-3.2 data)**

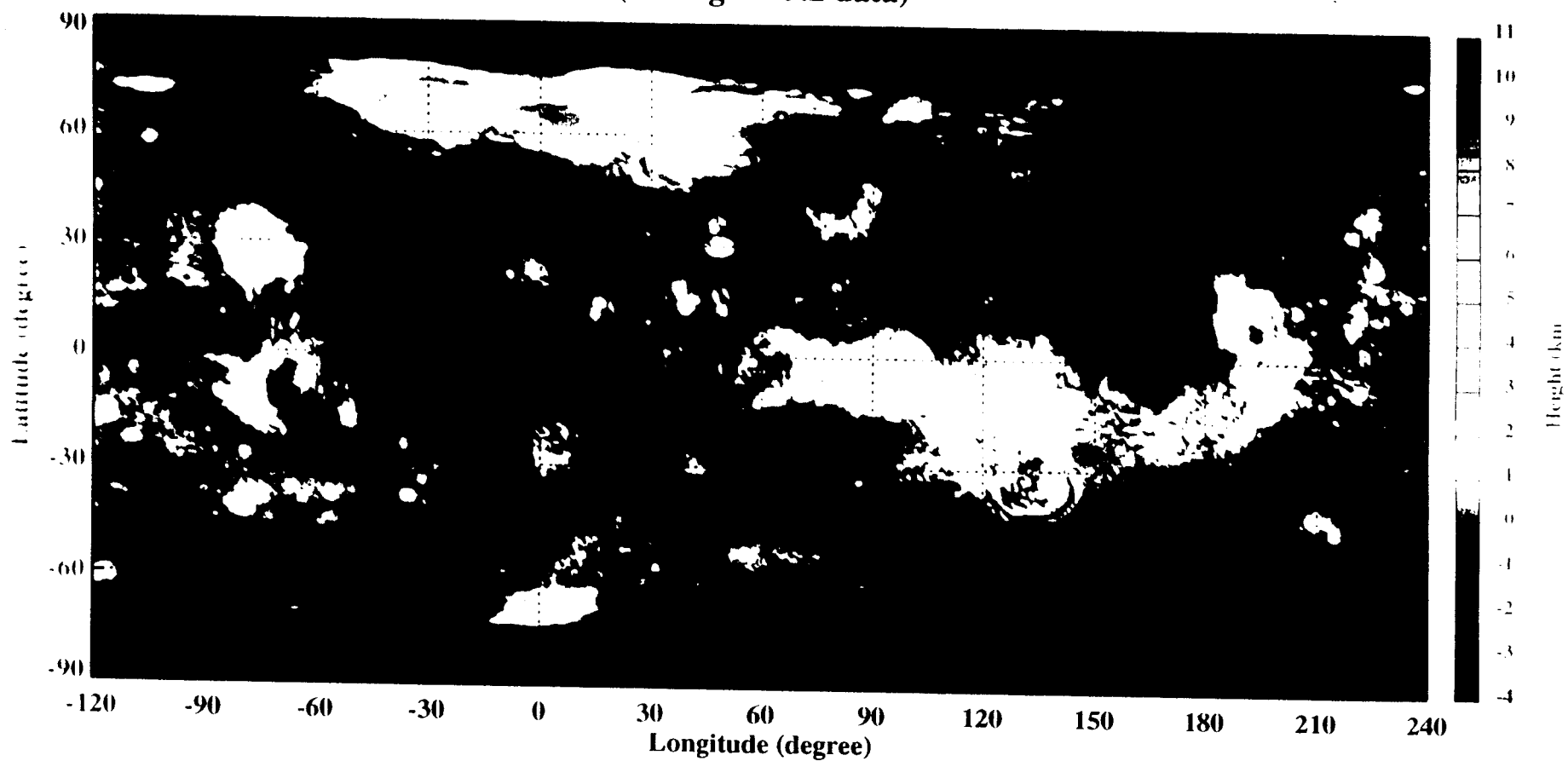


FIGURE 4

0 deg latitude

Continuous line = new observations, x = computed from new model

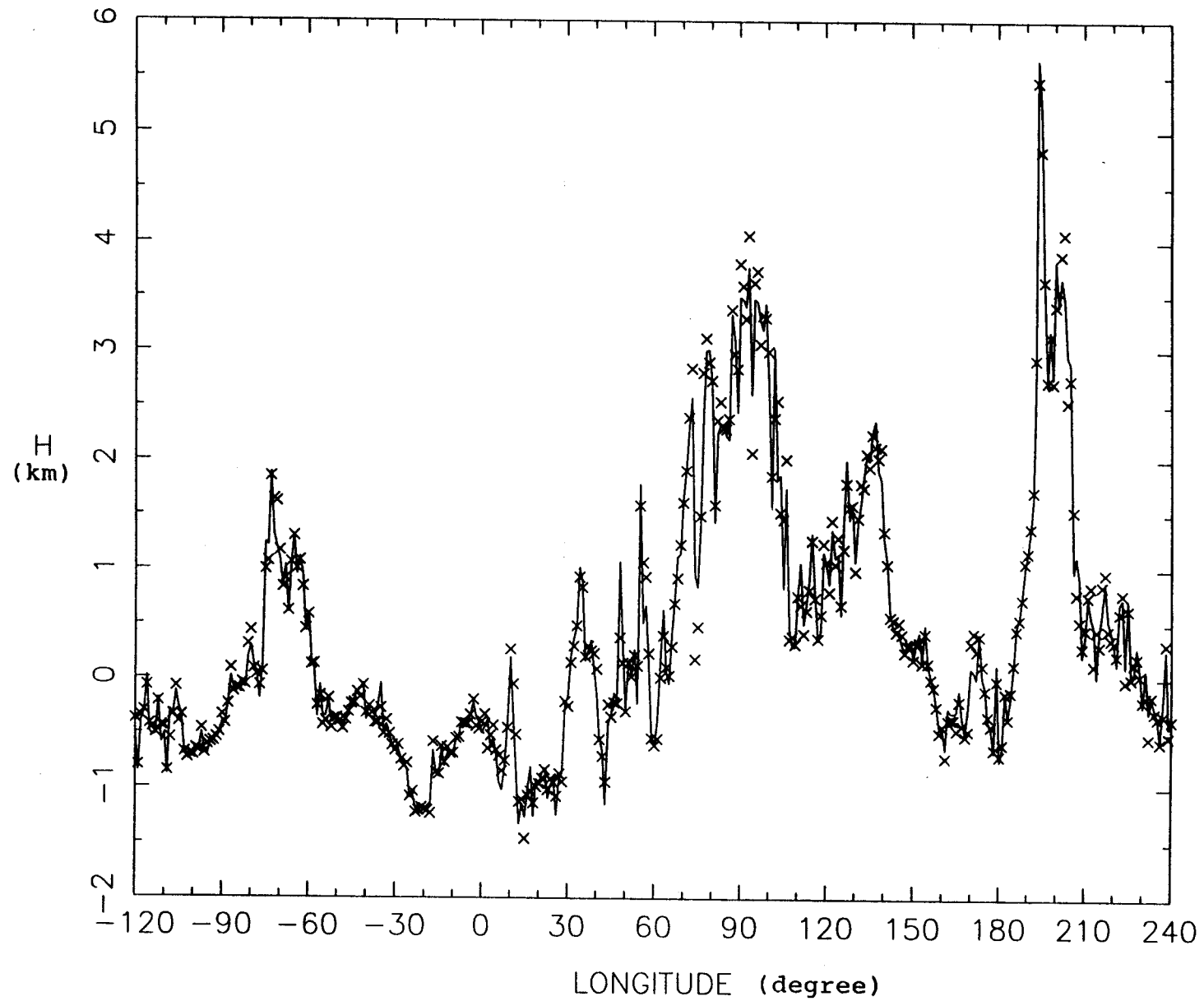


FIGURE 5

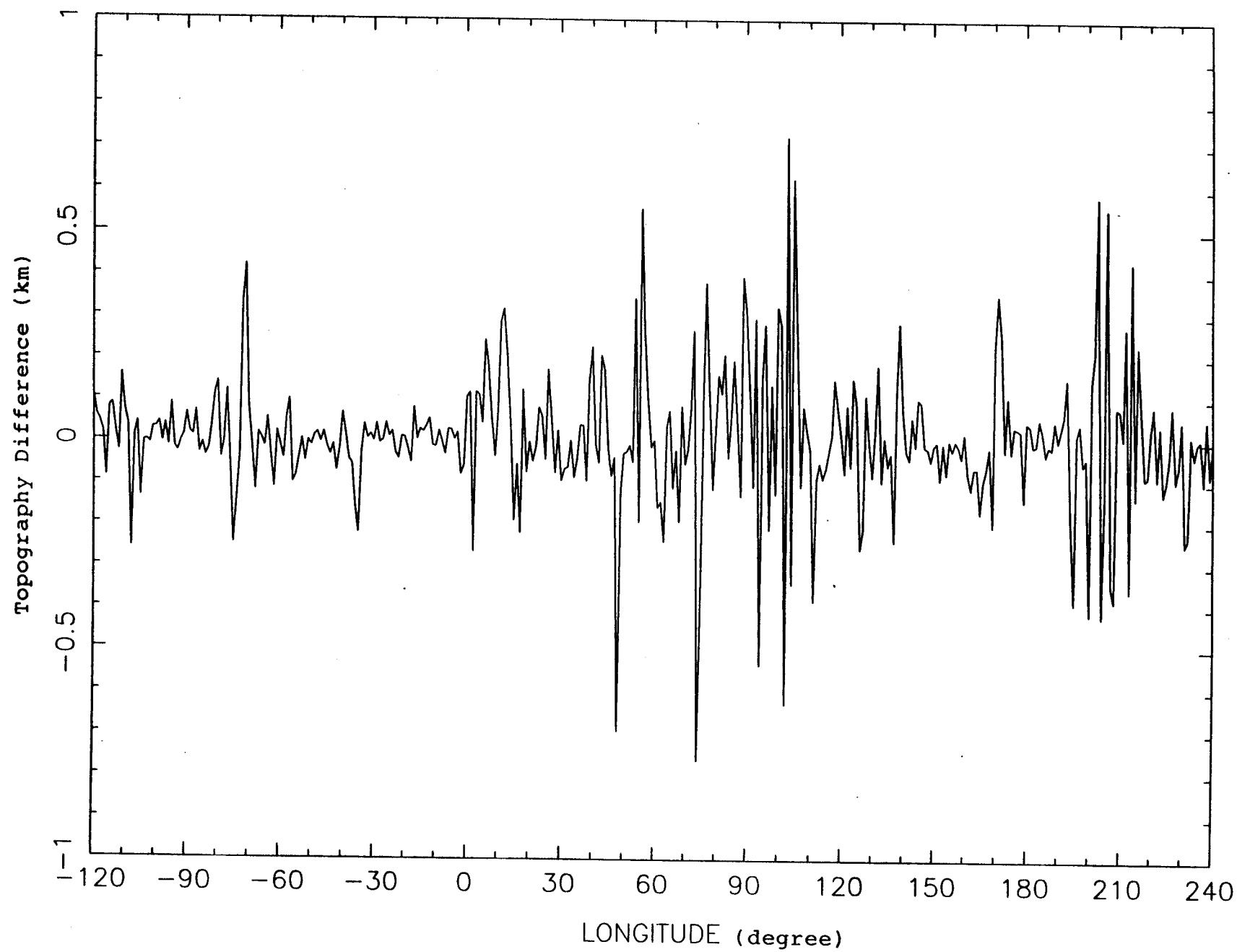


FIGURE 6

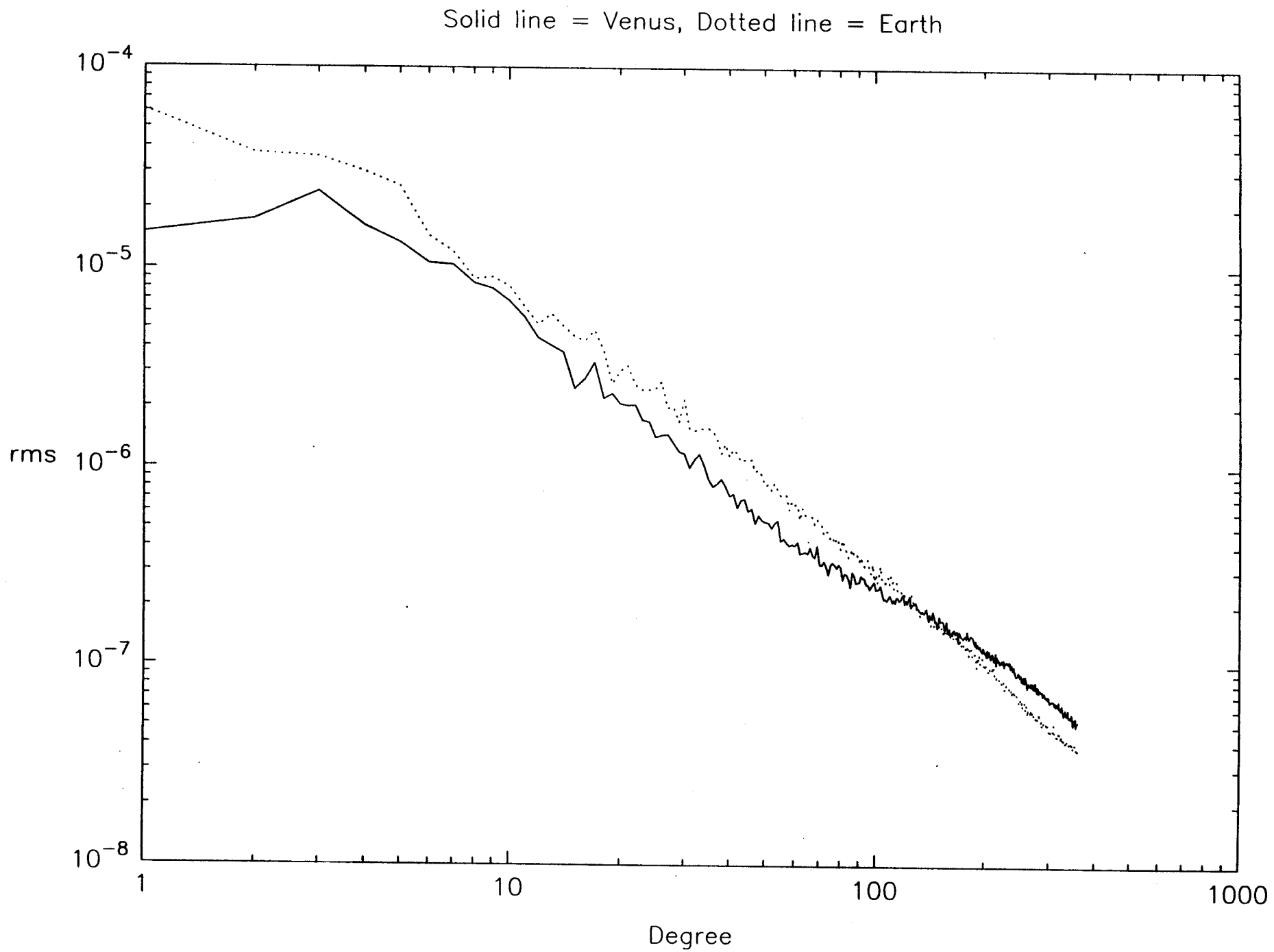


FIGURE 7

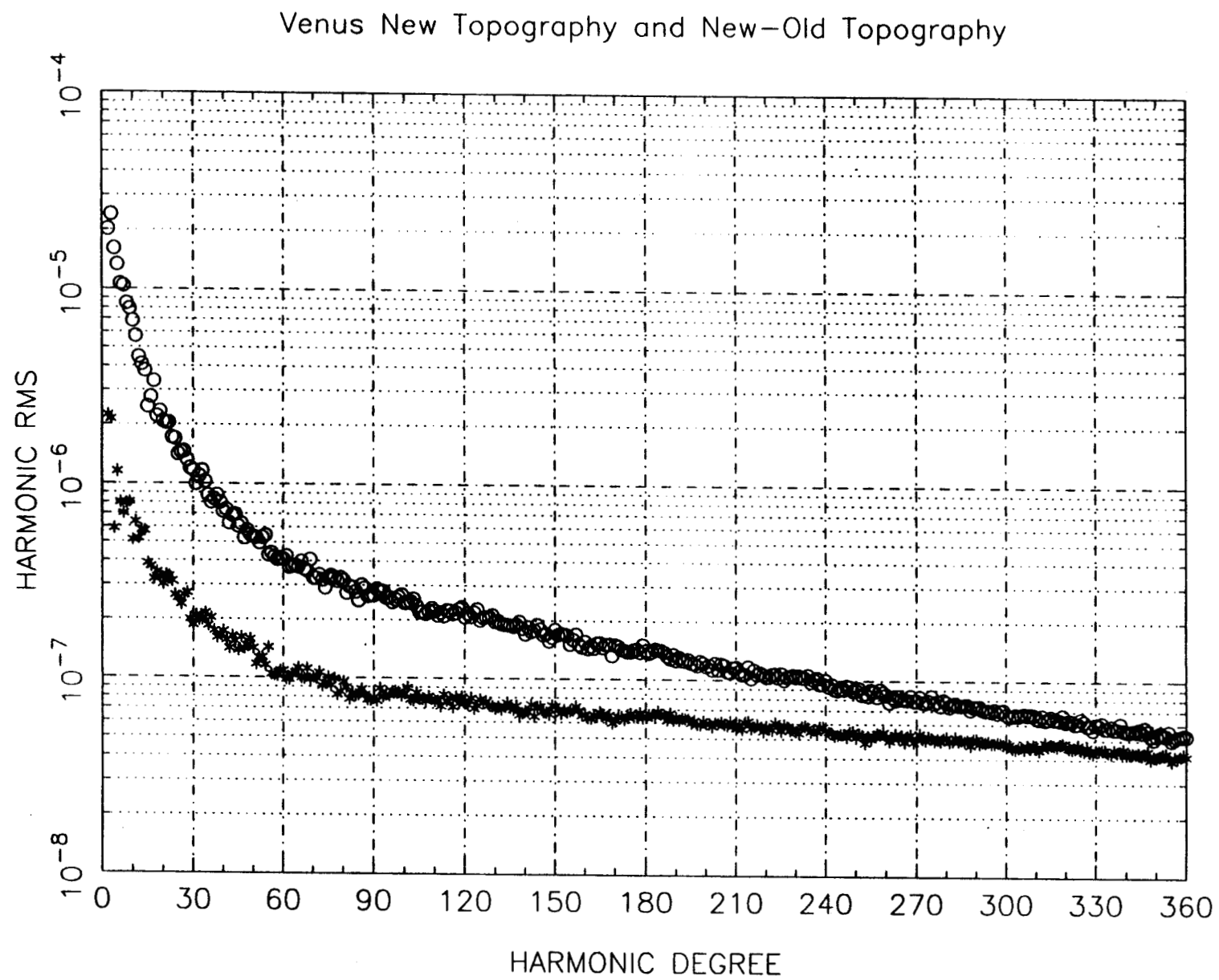


FIGURE 8

Topography - Gravity Correlations  
Solid line = new topo model, dotted line = old topo model

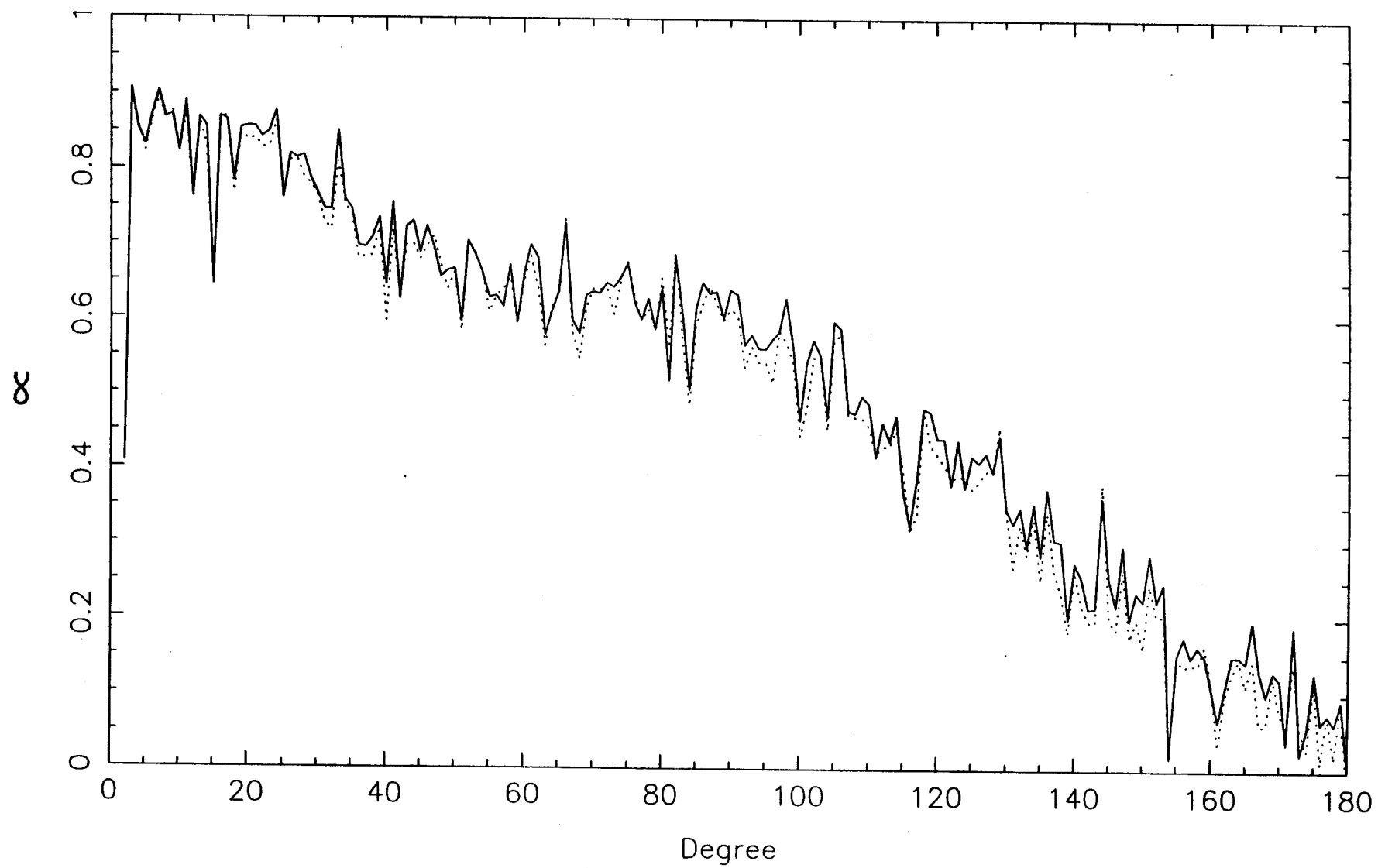


FIGURE 9



Geoid to topography ratios (GTR) per degree  
Circles correspond to observed data  
Line corresponds to uncompensated geoid

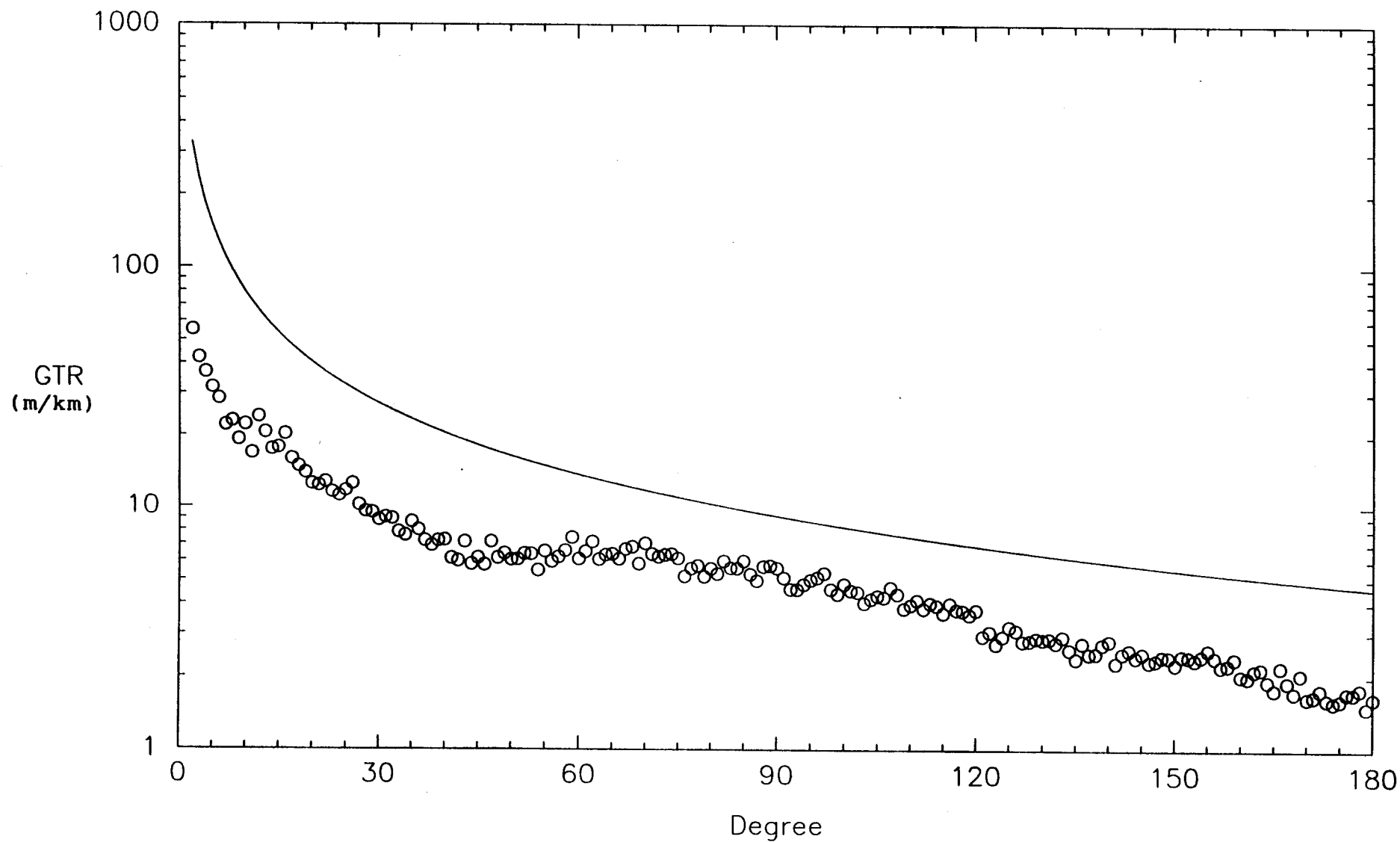


FIGURE 10